Searching for the first galaxies in the MUSE Extremely Deep Field

Cheryl Lüssi

May 14, 2021

Semester project in experimental physics, ETH Zurich
Supervisor: Prof. Dr. S. Lilly, Dr. J. Matthee

ABSTRACT

We study the spectra of Lyman-α-emitters (LAE) in the MUSE Extremely Deep Field (MXDF) in the redshift interval 2.86 to 4.6, with particular focus on low metallicity targets with a He-II $\lambda 1640$ peak, in order to find potential host galaxies of population III stars. Out of this catalogue, we report four such targets with identification numbers 88, 204, 435 and 22429 at redshifts 2.95, 3.14, 3.72, and 2.93 respectively. In the spectra of these targets, we look for metal peaks, such as C III] $\lambda 1909$, C IV $\lambda 1548$, O III] $\lambda 1666$ and Si III] $\lambda 1883$ in order to exclude active galactic nuclei (AGN) and galaxies with Wolf-Rayet stars or pair-creation supernovae (SN). todo: nr and iden

Contents

1 INTRODUCTION

The epoch of reionization, starting at a redshift $z \sim 20$ when the Universe was about 150 million years old, is described by the begin of formation of the first stars that emitted radiation strong enough to ionize the gaseous surroundings, whose baryonic content is predominantly H, He and small traces of heavier elements such as Li. As the gas itself was free from CNO-elements, the yet to be confirmed model for the first stars assumes a metallicity of $Z = 0$, referred as Pop-III stars. Pop-III stars can be classified into two groups, Pop-III.1 and Pop-III.2, [4]: the first group are believed reach masses up to $\sim 1000 M_{\odot}$ by accreting mass of their surroundings. As a result of their large masses, they must have strongly emitted in the UV-range, thus creating Strömgren-spheres with radii of a few kpc. In the end of their evolutionary history, they could have evolved into black holes of intermediate masses, IMBH, after exploding in supernovae, and thus enriching the Universe with heavy elements. In this model, the second type of Pop-III stars formed within the Strömgren-spheres of Pop-III.1 stars. In the environment of Pop-III.1 stars, molecules, such as hydrogen-deuteride formed, which cools the gas. As a result, the Pop-III.2 stars have a much lower mass compared to the former ones, $M_{III.2} \sim 50 M_{\odot}$. Other sources estimate the masses of Pop-III stars $M_{III} > 100 M_{\odot}$, e.g. [19].

As the goal of this work is to find galaxies that potentially have such Pop-III stars, we study the spectra of Lyman-α emitters, hereafter denoted with LAE. The Lyman-α emission line is caused by the transition of the electron in the hydrogen atom from the state $n = 2$ to $n = 1$, where n denotes the principal quantum number, and is the first line in the Lyman-series. The resulting wavelength of this transition has a rest-wavelength of $\lambda = 1215.67\text{Å}$. Due to the fine-structure splitting of the ($n = 2$, $l = 1$)-state into $j = \frac{1}{2}$ and $j = \frac{3}{2}$, the Lyα-peak is a double-peak with corresponding wavelengths 1215.668Å and 1215.674Å. Here, we do not focus predominantly on this peak and so we use $\lambda_{Ly\alpha} = 1215.67\text{Å}$. Therefore, in order to ionize neutral hydrogen, a wavelength shorter than $\lambda = 912\text{Å}$ is required and several different objects have been observed to emit such radiation: large O- and B-stars, which have a high luminosity, according to the relation $L \propto M^3$, where M is the mass of the star, and are short-lived, $\tau \propto \frac{M}{L} \propto \frac{1}{M^2}$. Due to their high luminosity, the spectrum is in the UV-range, hence they can act as LAEs. Another source of radiation with $\lambda \leq 912\text{Å}$ are AGN and quasars, e.g. [18]. The high emission originates from the accretion disk, in which charged particles are highly accelerated due to the presence of magnetic fields. These particles emit radiation in the X-ray-, IR- and UV-range that is collimated into jets perpendicular w.r.t. the accretion disk. We will discuss the origin of other diagnostic spectral lines, mainly the He II $\lambda 1640$ emission line, later.

Since the data in this work is measured by using a ground based telescope, see discussion in Section 2.1, the spectra of the targets show sky lines, see fig. 2 marked in black. These lines are of special importance for the selection of targets according to the He II $\lambda 1640$ peak, since they can coincide. In such cases, large uncertainties is to be expected and in most studies, such targets have been discarded, [18] and [20]. The analysis of spectral lines Lyα, He II $\lambda 1640$ and C IV $\lambda 1548$ is further complicated by the fact that these lines are resonant, [10], i.e. the photons emitted by the source can be absorbed and re-emitted again during their travel, which effects the measured flux density. This problem is adressed in section 2.3.

The paper is arranged in the following way: In Section 2, we briefly discuss the details of the survey and the following process of data reduction in order to identify potential Pop-III host galaxies. In Section 4 we analyse the spectra of the chosen targets in depth, focusing mainly on the He II $\lambda 1640$ peak by discussing different origins of this emission line and whether they are relevant for our sample. For that purpose, we create line ratio plots and determine the signal-to-noise ratio, SNR, as well as the integrated flux of the emission lines and the full widths at half maximum, FWHM. In Section 5, we summarize the main aspects and conclusions of this work. The fitted C III] $\lambda 19009$, C IV $\lambda 1548$, O III] $\lambda 1666$ and Si III] $\lambda 1883$ emission lines, if existing, for the selected targets can be found in the appendix. Throughout this work, we assume a flat ΛCDM model with $\Omega_m = 0.3$, $\Omega_{\Lambda} = 0.7$ and $H_0 = 67.7 kms^{-1} Mpc^{-1}$ as given by [1].

2 METHODS AND DATA REDUCTION

2.1 MUSE Extremely Deep Field

Here, we briefly summarize the main aspects of the survey description. For a more detailed discussion, the reader is referred to [18] and [16].

The data used in this work is from the MUSE Extremely Deep Field, which lies within the Hubble Ultra-Deep Field, and has a maximum observation depth of 140 hours, [18], using the Very Large Telescope (VLT) GALACSI/AOF Ground-Layer Adaptive Optics system, [2] and [3]. In order to improve the data collection, the telescope was rotated between observations, yielding a circular field of view, see fig. 1. The outer part between radii 31" and 41" has therefore only a short exposure time of $\mathscr{O}(10)$ hours and the data from this area is not included in the catalogue due to the resulting large systematic errors. The field of view up to a radius 31" has an exposure time of $\mathscr{O}(100)$ hours. The measured data is collected in a catalogue of 1574 targets. From this catalogue, a subset of 724 targets is extracted by selecting only galaxies for which the corresponding redshift could be determined with high confidence. The total sample covers a nominal wavelength range from 4700Å to 9350Å. In this work, we will use this reduced catalogue.
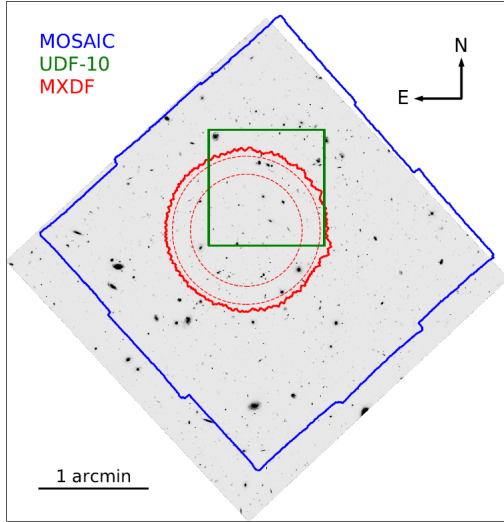
Table 1: Rest-frame wavelengths for different peaks from [10]. For the O III] peak, we choose the second one, marked by †, [16].

peak	wavelength [Å]
$Ly\alpha$	1215.67
C IV	1548.19
He II	1640.42
O III]	1660.81
O III]†	1666.15
[C III]	1906.68
C III]	1908.73
Si III]	1882.71

2.2 Line identification

The process in this subsection follows mainly the steps described in [20].

First, we shift the spectra for each galaxy to the rest-frame using the redshifts from the catalogue, and determine the wavelength range where we expect to find LAEs with a He II $\lambda 1640$ peak, see [27]. To do so, we convert the wavelength boundaries into redshift boundaries for the Lyα and the He II $\lambda 1640$,

$$z = \frac{\lambda_{obs} - \lambda_{emit}}{\lambda_{emit}}. \qquad (1)$$

The resulting redshift range is $z \in [2.86,\ 4.7]$. For all these targets, the two peaks are then collected in a separate FITS file.

In the next step, we visually inspect the wavelength regimes where we expect the Lyα peak and the He II $\lambda 1640$ peak and discard all targets that do not show one of these two peaks. The result is given in table 2.

The remaining ones are modelled with a single Gaussian fit using *lmfit*, which is a python module that provides a high-level interface to non-linear optimization and curve fitting problems. The advantage of *lmfit* which will benefit us is the ability to add parameters in a dynamical way. For further documentation, the reader is referred to [24]. The parameters of the Gaussian fit are the amplitude, position, standard deviation and a continuum level; the latter to account for the stellar continuum, which we subtract from the peak, see for example figure 4. As briefly mentioned in Sec. 1, we discard all targets where the He II $\lambda 1640$ peak coincides with a sky line. In this step, we also discard all targets whose spectra show a negative mean flux density in the wavelength range $\lambda \in [1610,\ 1670]$Å and a He II velocity offset $\Delta v_{HeII} \notin [-800, 500]\ km/s$. In

Figure 1: Location of the MXDF. The innermost circle describes the area with a $\mathscr{O}(100)$ hour exposure time, [18].

For all wavelengths in the rest-frame, we use the values given in [10], which we list in table 1.

choosing these boundaries, we assure that we only look at shifted He II $\lambda 1640$ peaks and ignore peaks from other elements, which will be discussed later. Note, that the interval towards red wavelengths is larger than the blue side, which is due to the ???. The selected targets are listed in table 2. MENTION THAT WE BOOTSTRAP THE FLUX DENSITIES OF THESE GALAXIES => MAIN PART3

Next, we focus on the presence of heavier elements in the spectra of the above selected targets. As discussed in [20] and [11], both He II and C IV emissions are found to be preferentially emitted by low-metallicity galaxies that are powered by star-formation. However, the presence of broad C IV emission lines is not only an indicator for low-metallicity star-formation, but also for AGN activity, [20]. We therefore plot and visually inspect the C IV $\lambda 1548$ line for these targets. This line results form the emission of C^{++}-ionizing photons, which require an energy $E_{C\ IV} \geq 47.89$ eV, which is lower than the ionizing potential for He II. For galaxies in the sample that show a significant C IV peak, we therefore have to discuss whether this peak arises from AGN activity.
Following [16], we then inspect the C III] $\lambda 1909$, O III] $\lambda 1666$ and Si III] $\lambda 1883$ peaks; the first one being a result of C^+-ionizing photons with $E_{C\ III]} \geq 24.38$ eV, what are OIII] and SiIII] results of?. The results are given in table 2. We note, that for target 538 the C III] $\lambda 1909$ and the Si III] $\lambda 1883$ emission lines were not measured.
We create two line-ratio diagrams,

$$\left(\frac{Si\ III]}{C\ III]}, \frac{C\ III]}{O\ III]} \right)$$
$$\left(\frac{O\ III]}{He\ II}, \frac{C\ III]}{He\ II} \right).$$

The second one has been suggested to identify whether the source of the ionising photons has stellar or AGN origin, [6]. The results are shown in figure 5. Considering ratios between resonant emission lines decreases the uncertainty in the measured flux densities due to dust attenuation, which can have a significant effect on resonant emission lines, see Section 4.2.

2.3 Line measurement

what comes in this subsection?
Having extracted the Lyα and He-II $\lambda 1640$ peak for each target with the constraints mentioned in Sec. 2.3, the number of possible Pop-III star host galaxies is reduced by filtering out targets that do either not show a Lyα peak or with no significant He-II $\lambda 1640$ peak. The computed signal-to-noise ratios (SNR) and integrated fluxes are given in table 3.

For the remaining targets, we compute the SNR and integrated fluxes for the peaks C III] $\lambda 1909$, C IV $\lambda 1548$, O III] $\lambda 1666$ and Si III] $\lambda 1883$. The results are shown in table 3.

3 RESULTS

In this section, we first list the selected targets with their corresponding redshift and give an overview which emission lines they feature, see table 2. For the targets we discuss, the spectra are plotted. In Section 3.2, we show the single Gaussian fitted He II $\lambda 1640$ emission lines as well as the SNR and the integrated flux of the targets, see table 3, where we also show the results for the Lyα, C III] $\lambda 1909$, C IV $\lambda 1548$, O III] $\lambda 1666$ and Si III] $\lambda 1883$ emission lines. Finally, the FWHM for the same peaks are given in table 4. All calculations can be found in [27].

3.1 Selected targets

In table 2, we list the targets that have been selected after visually identifying a He II $\lambda 1640$ peak. The first column, *iden* refers to the target's identification number in the data cube, see Section 2.1. An observed peak is marked with *x*, while - implies that no peak in the respective wavelength range has been observed. Due to the high redshift of target 538, the C III] and Si III] peaks are not detected, see equation (1), which we mark with *o*. In the figures 2 and 3 we show the complete detected spectra, shifted to the rest frame, of some targets listed in table 2, on which we focus the discussion.

Table 2: Selection of targets from the catalogue that are further analysed in this work: the sample consists of the targets that show a He II λ1640 peak. We examine the existence of the following other peaks: Lyα, C III] λ1909, C IV λ1548, O III] λ1666 and Si III] λ1883. For the target 538, two peaks were not be measured by MUSE and are marked with "o".

| iden	z	ra	dec	Lyα	He II	C III]	C IV	O III]	Si III]
48	2.9101489	53.169377597615	−27.7940364140812	x	x	-	-	-	-
88	2.9541607	53.1580734608277	−27.7944264427115	x	x	x	-	x	-
118	3.0024831	53.1682775257735	−27.7810365663019	x	x	x	x	x	x
131	3.0191996	53.1571730528989	−27.7803069343136	x	x	x	-	x	x
204	3.1357558	53.1714481954865	−27.7848694395671	x	x	-	x	-	-
218	2.865628	53.1708826995566	−27.7831473048059	-	x	x	x	x	-
435	3.7247474	53.1679218127805	−27.7786955004121	x	x	x	x	x	-
538	4.1764603	53.1657960632343	−27.781314653307	x	x	o	-	-	o
5199	3.063	53.1670692	−27.79018751	x	x	-	-	x	-
7876	2.993115	53.16627152	−27.77985137	-	x	x	-	x	-
22429	2.9297342	53.17097057	−27.78715696	x	x	-	-	-	x
23124	3.5935392	53.16233266	−27.79300494	x	x	-	x	-	-
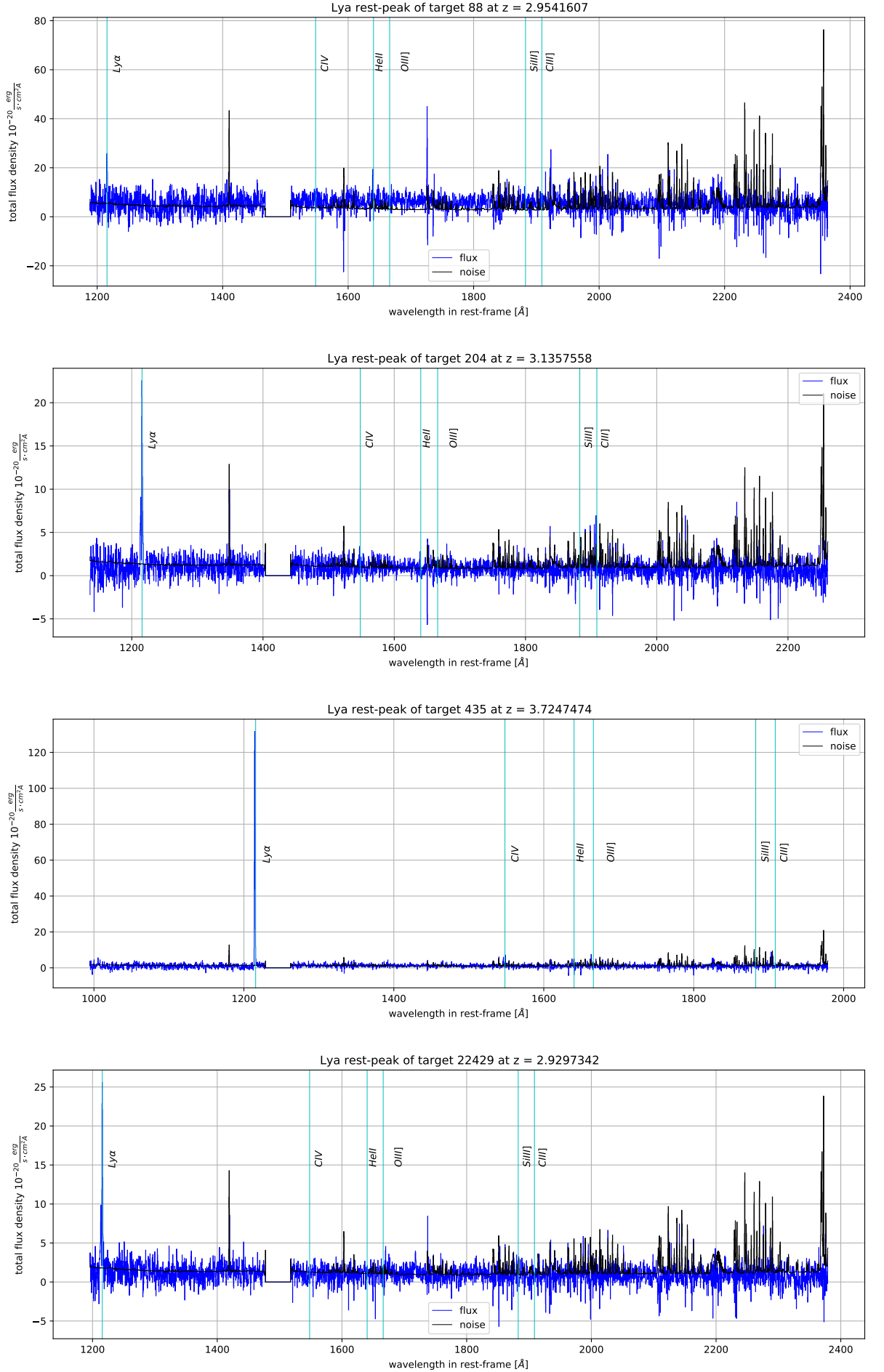
Figure 2: Spectra of the targets 88, 204, 435, and 22429 shifted to the rest-frame. The flux density is given in blue, the noise due to sky lines is shown in black. The vertical lines mark the position of the Lyα, He II $\lambda1640$, C IV $\lambda1548$, O III] $\lambda1666$, Si III] $\lambda1883$ and the C III] $\lambda1909$ peak, [27].
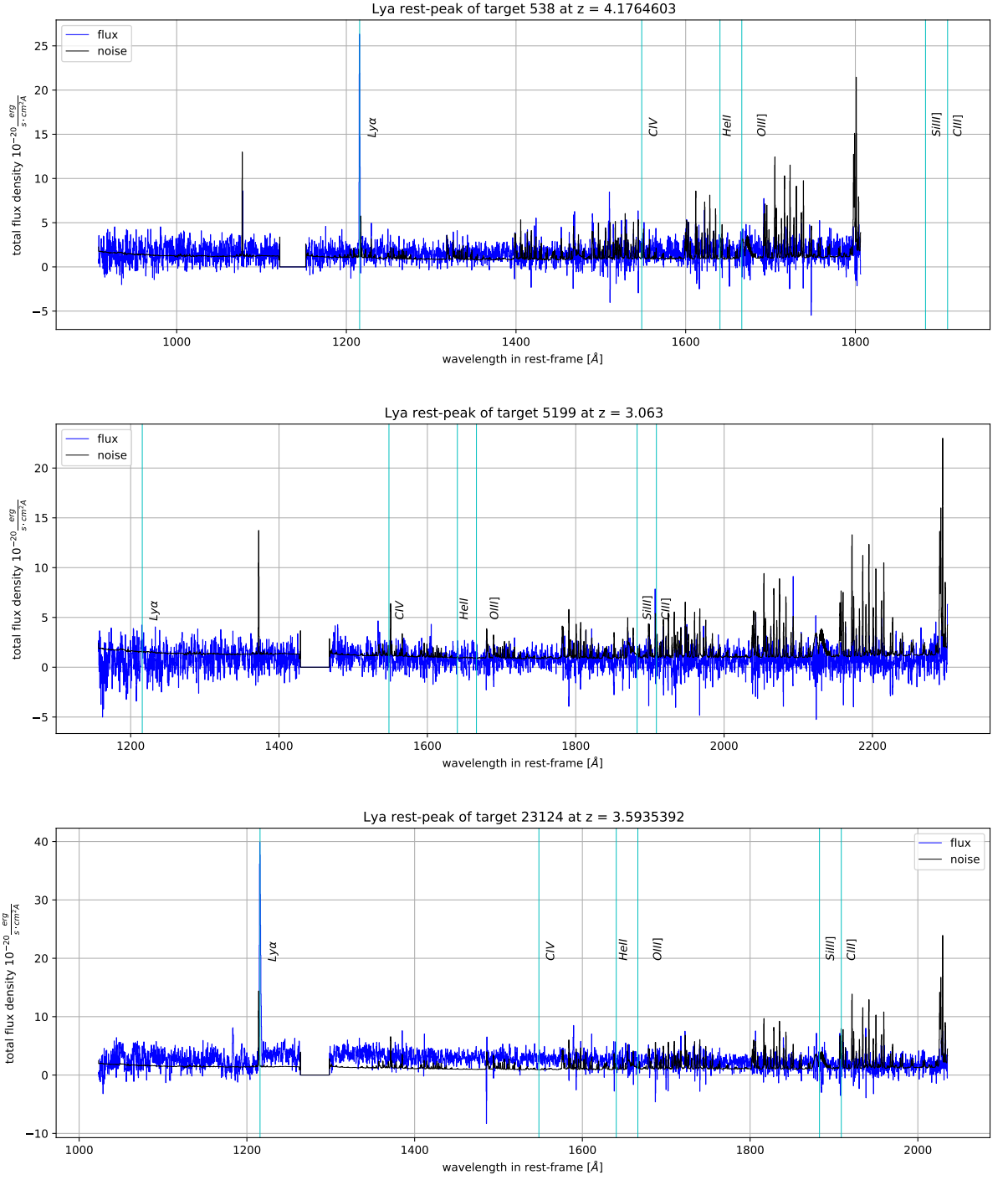
Figure 3: Spectra of the targets 539, 5199 and 23124 shifted to the rest-frame. The flux density is given in blue, the noise due to sky lines is shown in black. The vertical lines mark the position of the Lyα, He II λ1640, C IV λ1548, O III] λ1666, Si III] λ1883 and the C III] λ1909 peak, [27].

3.2 He II λ1640 emission lines

In figure 4, we present the He II λ1640 emission lines for the selected targets, see Section 2. The corresponding SNRs and integrated fluxes are given in table 3.
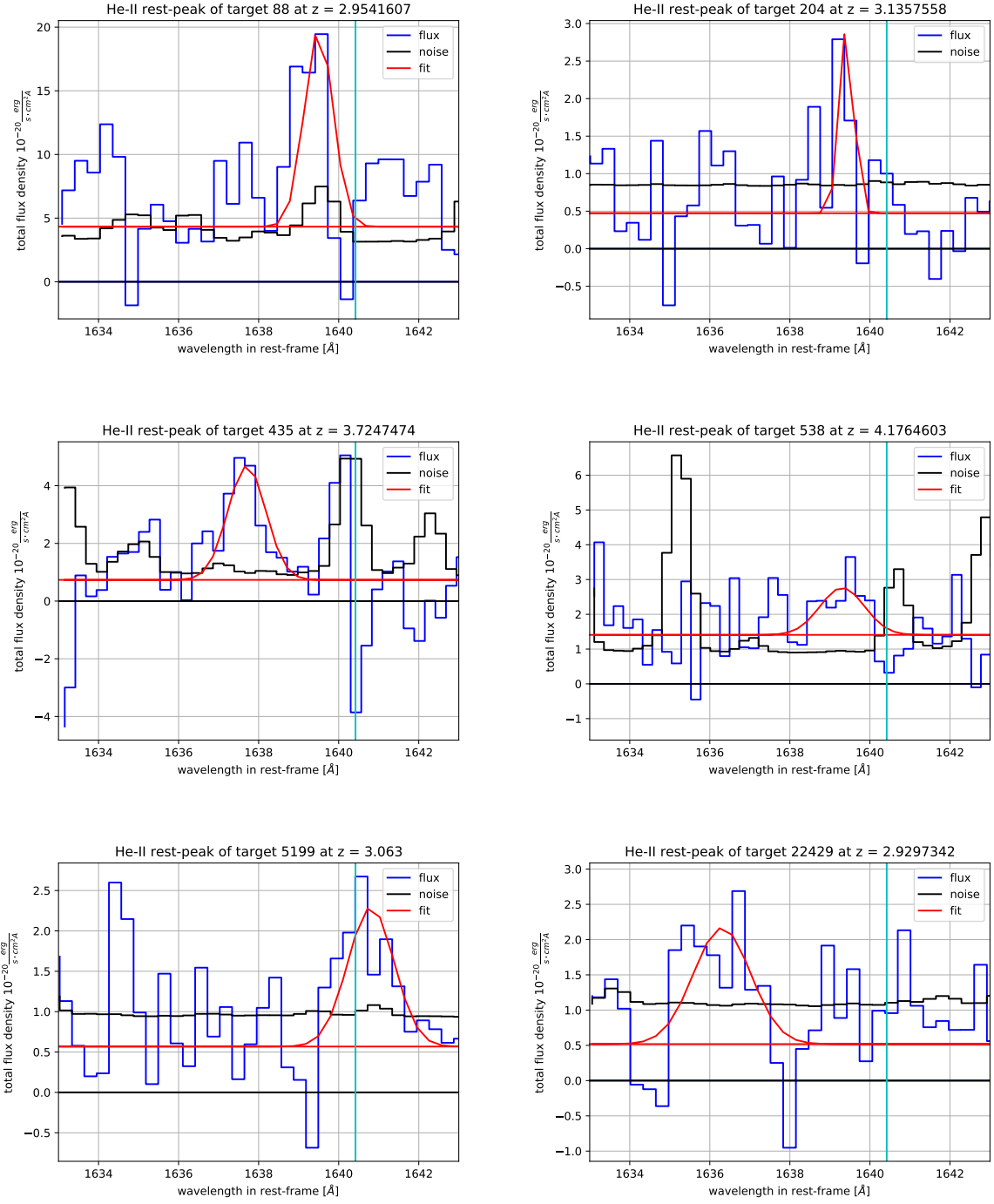
Figure 4: Single-Gaussian fitted He II $\lambda 1640$ emission line for the targets 88, 204, 435, 538, 5199 and 22429, [27].

Table 3: SNR and integrated flux (in $\frac{10^{-20}erg}{s \cdot cm^2}$) for our target sample, rounded to one decimal place, [27]. Note that for the integrated flux in the case of a double-peak, we calculate the area under the dominant peak, which can affect the results especially for the Lyα line, see Section 4.3.

iden	Lyα		He II		C III]		C IV		O III]		Si III]	
48	4.0	22.8	2.8	5.3	—	-	—	-	—	-	—	-
88	4.7	54.4	2.6	21.3	3.5	3.1	—	-	2.5	10.3	—	-
118	75.5	227.2	5.2	11.0	6.1	15.2	7.3	15.3	8.9	58.7	5.8	16.1
131	13.5	48.5	4.7	6.7	6.9	15.4	—	-	6.3	43.0	4.6	10.7
204	16.2	41.7	3.3	1.8	—	-	3.5	15.3	—	-	—	-
218	—	-	4.0	10.9	4.4	29.6	2.3	c4	4.4	33.2	—	-
435	84.8	125.5	4.9	7.9	6.0	7.2	5.8	7.1	3.6	8.7	—	-
538	23.5	28.5	4.4	5.2	o	o	—	-	—	-	o	o
5199	2.6	4.0	2.6	3.8	—	-	—	-	2.9	11.8	—	-
7876	—	-	4.5	7.3	3.7	4.8	—	-	3.8	15.8	—	-
22429	13.6	36.1	2.7	3.9	—	-	—	-	—	-	3.0	2.7
23124	26.2	a	4.2	6.7	—	-	4.4	todo	—	-	—	-

3.3 FWHM

Table 4: Full width half max (FWHM), in Å rounded to two decimal places, for He II λ1640, C III] λ1909, C IV λ1548, O III] λ1666 and Si III] λ1883 emission lines of our sample, using the single Gaussian fit, [27].

iden	FWHM He II	FWHM C III]	FWHM C IV	FWHM O III]	FWHM Si III]
48	0.93	—	—	—	—
88	0.84	0.22	—	0.81	—
118	0.95	0.88	0.82	1.20	1.53
131	0.90	1.24	—	0.70	1.31
204	0.42	—	0.61	—	—
218	2.35	1.00	c4	2.38	—
435	1.12	0.66	0.93	0.97	—
538	1.31	o	—	—	o
5199	1.36	—	—	o3	—
7876	0.97	0.52	—	o3	—
22429	1.68	—	—	—	0.67
23124	0.45	—	c4	—	—

4 ANALYSIS AND DISCUSSIONS

In this section, we analyse for the selected targets whether they are possible host galaxies for Pop. III stars. To do so, we discuss the generation of the He II λ1640 emission line by AGN activity, WR stars, stellar rotation and binary stars, X-ray sources, pair creation SN, radiative shocks and stripped stars. In each case, we first give a brief introduction on how these objects affect the measured He II flux and then discuss which of our selected targets show such spectral features. In the case of AGN, we include the discussion of the C IV peak.

4.1 Origin of the He II λ1640 line

In the following, we list the different origins of the He II λ1640 emission line and discuss whether their relevance for sample. This line results from the ionization of He^+-ions, which requires energies above $E_{1640}^{ion} = 54.4 \ eV$, corresponding to a wavelength $\lambda = 228$Å. It has been shown, [23], [22], that the He II λ1640 line is particularly sensitive to the metallicity and accordingly the equivalent width is $W(He \ II \ \lambda1640) \geq 5$Å only for $Z \leq 10^{-7}$.

4.1.1 AGN

As discussed in detail in [6], the rapid accretion rate of supermassive black holes (SMBH) contributes to the overall production of UV and optical nebular emission lines. In order to check whether our targets show AGN-activity, we determine whether the measured He II $\lambda 1640$ fluxes can be explained by star formation, following [16] and [20]. In addition, a broad C IV $\lambda 1548$ emission line is an indicator for the target to be powered by other sources than ongoing star formation, e.g. AGN. The C IV $\lambda 1548$ emission lines for the selected targets can be found in the appendix.

The C IV FWHM of our sample are given in table 4. Only the targets 118, 204, 435 and 23124 show such a spectral feature, none of them being broad enough to indicate a significant contribution of He^+-ionizing photons. We note however, that the targets 218, 5199 and 7876 have no (dominant) Lyα peak, see table 3 for the SNR of the Lyα peaks, which is an indication that these galaxies are not powered by star formation alone. FINISHED

4.1.2 WR stars

Wolf-Rayet stars are massive, large evolved stars (Pop. I) that have lost their hydrogen shell, thus exposing the helium fusing core. Their most prominent features are the strong stellar winds that cause broad He II $\lambda 1640$ emission lines, which we can use to determine whether WR-stars contribute significantly to our sample. In such a case, we expect a broad FWHM $\geq 1000 km/s$, [20] and [16]. As seen from table 4, none of these targets show such a large FWHM and we therefore cannot predict WR stars to contribute significantly to the total amount of He^+-ionizing photons. Finished

4.1.3 Stellar rotation and binary stars

As discussed in [16], the inclusion of binary star models increases the production of ionizing photons, which, on one hand increases the life time of massive O- and B-stars, and on the other hand increases the production of WR-stars. Stellar rotation causes rotational mixing within the star, that leads to higher effective temperatures (up to 90 kK in the hydrogen burning phase), [9] and [20]. As shown by [17], these two effects have to be considered together because binary interactions lead to increased stellar rotation. Important for our study is the observation that stellar winds are weaker in low metallicity stars which results in a more efficient stellar rotation, [9], which can cause more of the heavy elements, that are fused in the core, to be transported to the surface and an increased mass transfer between binary stars. In the case of fast rotation, we expect a strong helium enrichment on the stellar surface even in the core hydrogen burning phase, [9].

BPASS: falls short (check this for our sample) in explaining detected He II and CIII] fluxes but not the OIII] (check this). Mention the tool to determine whether this is the origin and analyse the sample spectra:

The Binary Population and Spectral Synthesis project (BPASS) is a code to combine different detailed stellar evolution models, in particular, to include the evolution of binary constellations, which result in a bluer appearance than for single stellar constellations only. For more details, teh reader is refered to [25] and the accompanied paper [26].

4.1.4 X-ray sources

In a binary constellation consisting of a black hole / neutron star / pulsar and a O-/ B-star, [12] have shown that the mass accretion onto the former one produces a large amount of hard ionizing photons. From the strength of the X-ray binary, the mass transfer rate is expected to be determined. [13] have shown, that in low-metallicity systems for a fixed stellar formation rate (SFR), the high X-ray luminosity could contribute significantly to the production of ionizing photons with energies above 54.4 eV. discuss

4.1.5 Pair creation SN

This type of supernova occurs when pair-production within the star reduces the internal radiation pressure, exerted by fusion processes. As a result, the gravitational pull temporarily exceeds the outward directed force and the star collapses partially. The density within the core increases, leading to a faster fusion rate, which causes a rapid expansion of the star and eventually a complete disintegration of the star. This phenomenon can only occur in massive stars with low to moderate metallicity [7]. During this supernova, heavy elements can be produced, [8].

4.1.6 Radiative shocks

In order to analyse a potential contribution to He^+-ionizing photons originating from radiative shocks, we follow [16]: we determine the He II $\lambda 1640$ SNR of our sample (the results are given in table 3) and use the result from [14] and [22], who showed that radiative shocks contribute more to He II $\lambda 1640$ in low-mass galaxies, since the outflow of mass per SFR is higher. The SNRs of our targets, see table 3, are all ≤ 5 and we therefore cannot make a prediction about the contribution of radiative shocks in our sample. FINISHED

4.1.7 Stripped stars

Stripped stars are low mass stars in a binary star configuration that loose a large amount of their H-shell, [5]. The subjacent helium shell, with higher temperature, can produce high energy photons, capable of ionizing He^+ ions and thus producing the characteristic He II $\lambda 1640$ spectral peak. Discuss probability of our peaks to originate form stripped stars.

The presence of metals in a star effects its emitted radiation due to scattering. With increasing metallicity, the emitted radiation from the H- and He-lines is partly absorbed by these heavy atoms and thus the equivalent width of the spectral lines decreases. need reference and more details on process.

4.2 Line ratios

As mentioned in section 1, the presence of dust affects the measured flux of resonant emission lines such as Lyα, He II $\lambda 1640$ and C IV 1548. Special care has therefore to be taken when interpreting these lines. The uncertainties however decrease when we look at the line ratios, rather than each line separately, [16]. In figure 5 we show the line ratios for the selected targets that show the corresponding spectral features, see table 2.
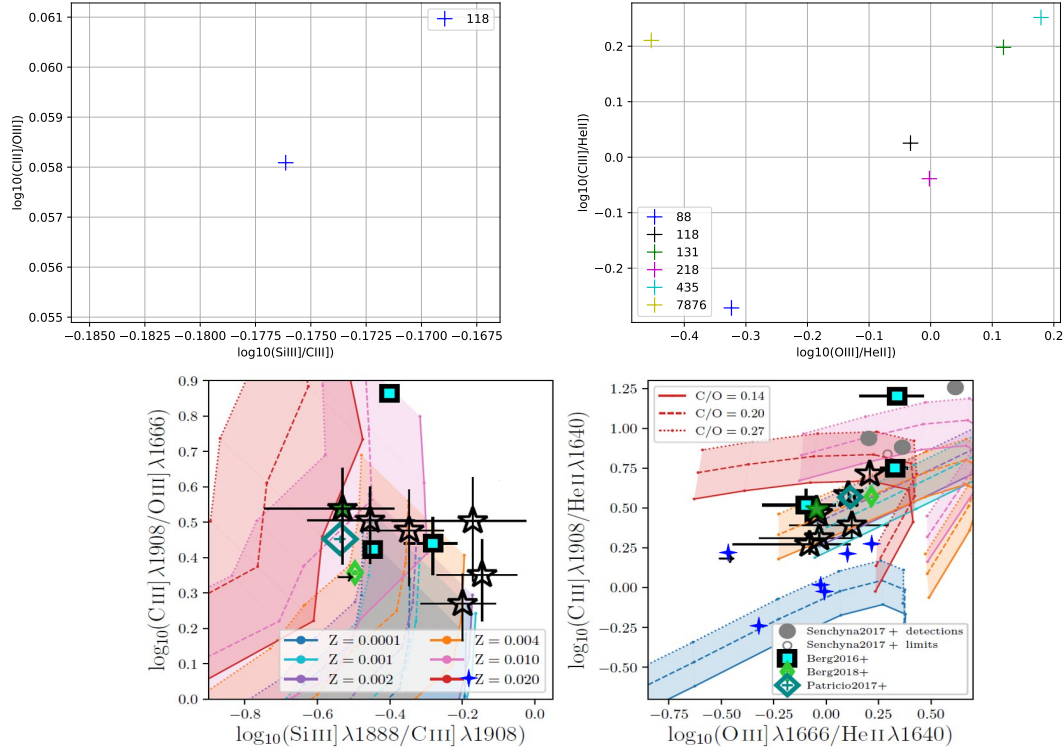

Figure 5: **Top:** Line ratio plots $\left(\frac{Si\ III]}{C\ III]}, \frac{C\ III]}{O\ III]}\right)$ and $\left(\frac{O\ III]}{He\ II}, \frac{C\ III]}{He\ II}\right)$ using He II $\lambda 1640$, C III] $\lambda 1909$, O III] $\lambda 1666$ and Si III] $\lambda 1883$, [27]. **Bottom:** The corresponding line ration plots (their figure 7) from [16] for comparison. The position of our targets are inserted. For more clarity we mark all with a blue star.

By comparing our measured line ratio $\left(\frac{O\ III]}{He\ II},\ \frac{C\ III]}{He\ II}\right)$ with figure 7 from [16], see figure 5, we find that the targets 88, 118 and 218 lie in the range with a low metallicity of $Z = 0.0001$, between $C/O = 0.20$ and $C/O = 0.27$. Targets 131, 435 and 7876 are above this regime and are therefore expected to have a higher metallicity, $Z > 0.0001$. Our targets have a lower ratio C/O than the ones studied in [16].

For target 118, we determine the line ratio $\left(\frac{Si\ III]}{C\ III]},\ \frac{C\ III]}{O\ III]}\right)$ and find that it lies within the range of $Z = 0.001$, shown in light blue in the lower left plot in figure 5.

4.3 SNR and integrated flux

Here, we discuss how we examine the uncertainties in the SNR computations. mention and explain bootstrap, cite nana.
mention the error in the integrted flux when only choosing the dominant peak in case of a double peak, 3

5 SUMMARY

- -
- -
- -

References

[1] Planck Collaboration, Ade, P. A. R., Aghanim, N., et al.,
Planck 2015 results. XIII. Cosmological parameters,
arXiv:1502.01589 [astro-ph.CO]

[2] Kolb, J., Madec, P.-Y., Arsenault, R., et al.,
ESO Adaptive Optics Facility Progress Report,
https://www.eso.org/sci/libraries/SPIE2012/8447-19.pdf

[3] Madec, P. Y., Arsenault, R., Kuntschner, H., et al.,
Operational Concept of the VLT's Adaptive Optics Facility and its instruments,
https://doi.org/10.1117/12.925111

[4] T. Ohkubo, et al.,
Evolution of Very Massive Population III Stars with Mass Accretion from Pre-Main Sequence to Collapse,
arXiv:0902.4573

[5] R. Kippenhahn,
Mass Exchange in a Massive Close Binary System,
1969, A& A, 3, 83

[6] A. Feltre, S. Charlot, J. Gutkin,
Nuclear activity versus star formation: emission-line diagnostics at ultraviolet and optical wavelengths,
arXiv:1511.08217v1 [astro-ph.GA]

[7] A. Heger, S. E. Woosley,
The Nucleosynthetic Signature of Population III,
arXiv:astro-ph/0107037v2

[8] S. E. Woosley, T. A. Weaver,
The Evolution and Explosion of Massive Stars. II. Explosive Hydrodynamics and Nucleosynthesis,
1995, ApJS, 101, 181

[9] D. Szécsi, N. Langer, et al.,
Low-metallicity massive single stars with rotation. Evolutionary models applicable to I Zwicky 18,
arXiv:1506.09132v1 [astro-ph.SR]

[10] D. A. Berg, D. K. Erb, M. W. Auger, A. Pettini, G. B. Brammer,
A window on the earliest star formation: extreme photoionization conditions of a high-ionization, low-metallicity lensed galaxy at $z \sim 2$,
arXiv:1803.02340 [astro-ph.GA]

[11] D. A. Berg, D. K. Erb, E. D. Skillmann et al.,
Carbon and Oxygen Abundances in Low Metallicity Dwarf Galaxies,
arXiv:1605.06152v1 [astro-ph.GA]

[12] D. R. Garnett, R. C. Kennicutt et al.,
He II Emission in Extragalacitc H II Regions,
Astrophysical Journal v.373, p.458; 1991ApJ...373..458G

[13] M. Brorby, P. Kaaret et al.,
Enhanced X-ray Emission from Early Universe Analog Galaxies,
American Astronomical Society, HEAD meeting # 15, id.120.05

[14] A. L. Muratov, D. Kereš et al.,
Gusty, gaseous flows of FIRE: galactic winds in cosmological simulations with explicit stellar feedback,
arXiv:1501.03155v2 [astro-ph.GA]

[15] K. K. Nilsson,
The Lyα Emission Line as a Cosmological Tool,
arXiv:0711.2199 [astro-ph]

[16] Nanayakkara, T., Brinchmann, J., Boogaard, L., et al.,
Exploing HeII λ1640 emission line properties at $z \sim 2 - 4$
arXiv:1902.05960v1 [astro-ph.GA]

[17] R. G. Izzard, S. E. de Mink, et al.,
Massice Binary Stars and Self-Enrichment of Globular Clusters,
arXiv:1302.0725v1 [astro-ph.SR]

[18] R. Bacon, D. Mary, T. Garel, et al.,
The MUSE Extremely Deep Field: the Cosmic Web in Emission at High Redshift,
arXiv:2102.05516 [astro-ph.CO]

[19] Lecture at University of Koeln,
Star formation in the Early Universe: Population III stars,
https://hera.ph1.uni-koeln.de/~ossk/star-formation/PopulationIII.pdf; (21.04.2021)

[20] A. Saxena et al.,
The properties of He II 1640 emitters at z 2.5-5 from the VANDELS survey,
arXiv:1911.09999 [astro-ph.GA]

[21] V. Bromm, R.P. Kudritzki, A. Leob,
Generic Spectrum and ionization Efficiency of a Heavy Initial Mass Function for the First Stars,
arXiv:astro-ph/0007248v2

[22] D. Schaerer,
The transition from Population III to normal galaxies: Ly-a and HeII 1640 emission and the ionising properties of high redshift starburst galaxies,
arXiv:astro-ph/0210462

[23] D. Schaerer,
On the properties of massive Population III stars and metal-free stellar populations,
arXiv:astro-ph/0110697

[24] *LMFIT: Non-Linear Least-Squares Minimization and Curve-Fitting for Python*,
https://lmfit.github.io/lmfit-py/

[25] J. J. Eldridge, E. Stanway, et al.,
BPASS - Binary Population and Spectral Synthesis,
https://bpass.auckland.ac.nz/index.html

[26] J. J. Eldridge, E. Stanway, et al.,
Binary Population and Spectral Synthesis Version 2.1: construction, observational verification and new results,
arXiv:1710.02154v1 [astro-ph.SR]

[27] C. Lüssi,

Code and graphical realisation using Python 3.9;

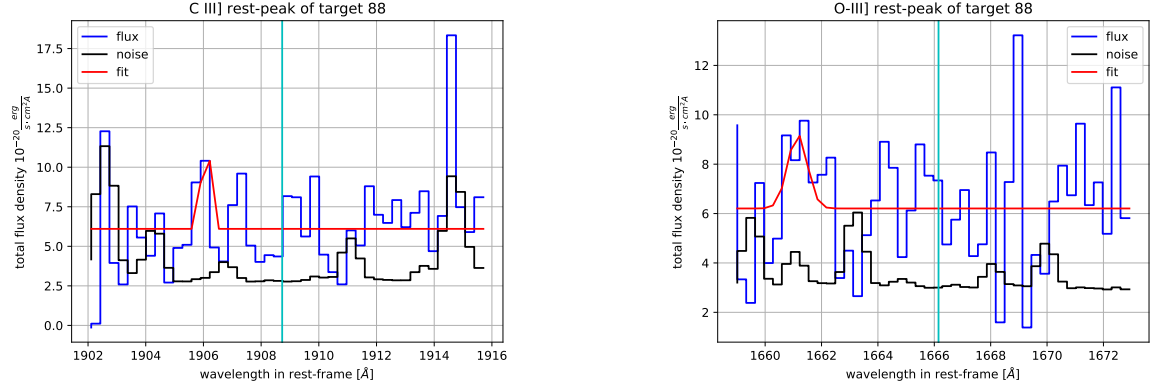Python code: https://github.com/Brillouin-Zone/astro.

6 Appendix

Figure 6: O III] $\lambda 1666$ and C III] $\lambda 1909$ emission lines of target 88, [27].
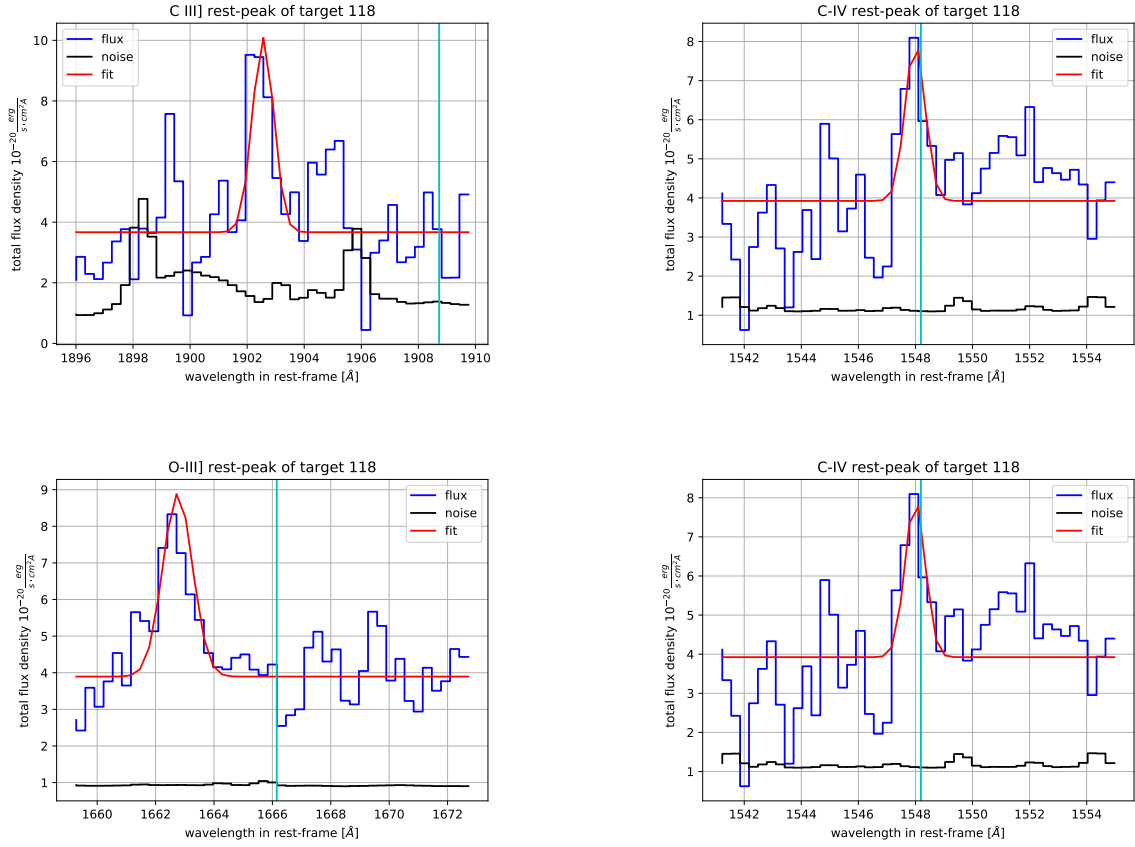
Figure 7: C IV $\lambda 1548$, O III] $\lambda 1666$, Si III] $\lambda 1883$ and C III] $\lambda 1909$ emission lines of target 118, [27].
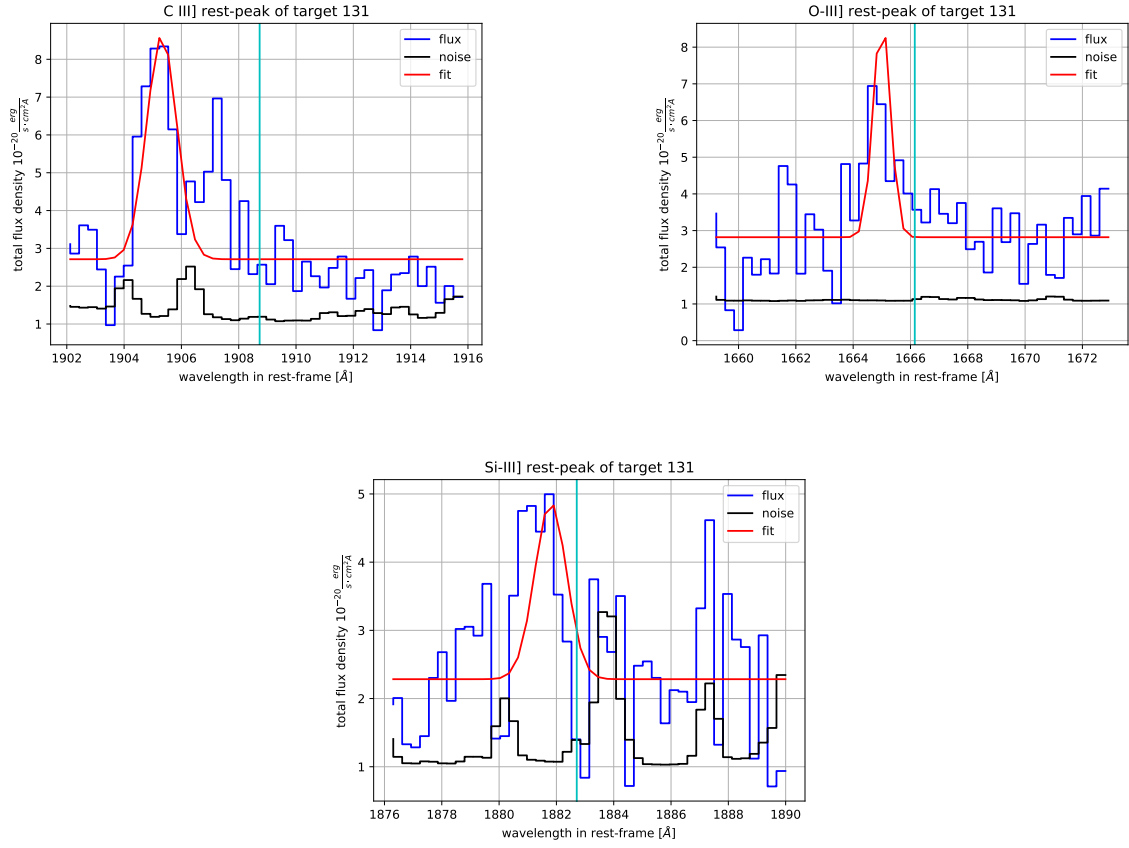
Figure 8: O III] λ1666, Si III] λ1883 and C III] λ1909 emission lines of target 131, [27].
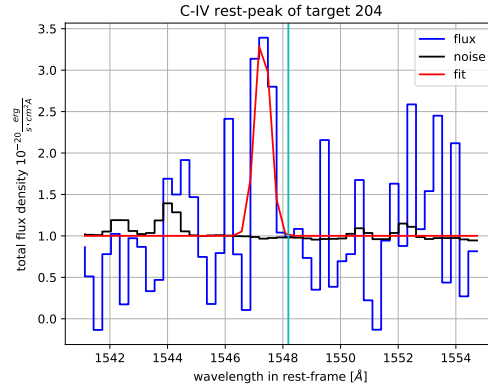

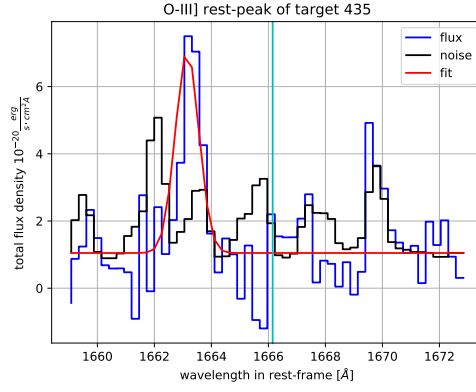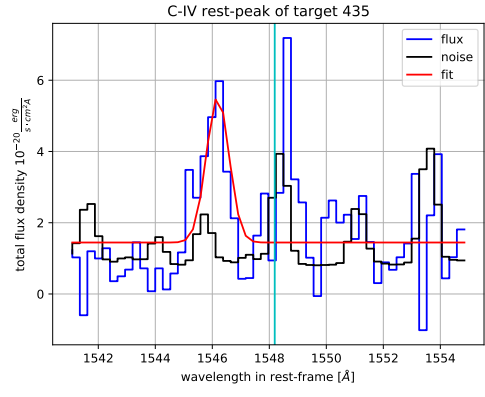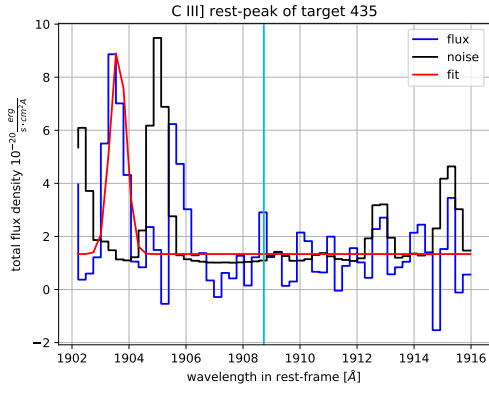Figure 9: C IV λ1548 emission line of target 204, [27].

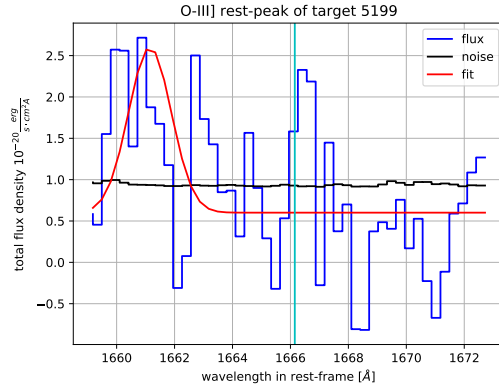Figure 10: C IV λ1548, O III] λ1666 and C III] λ1909 emission lines of target 435, [27].

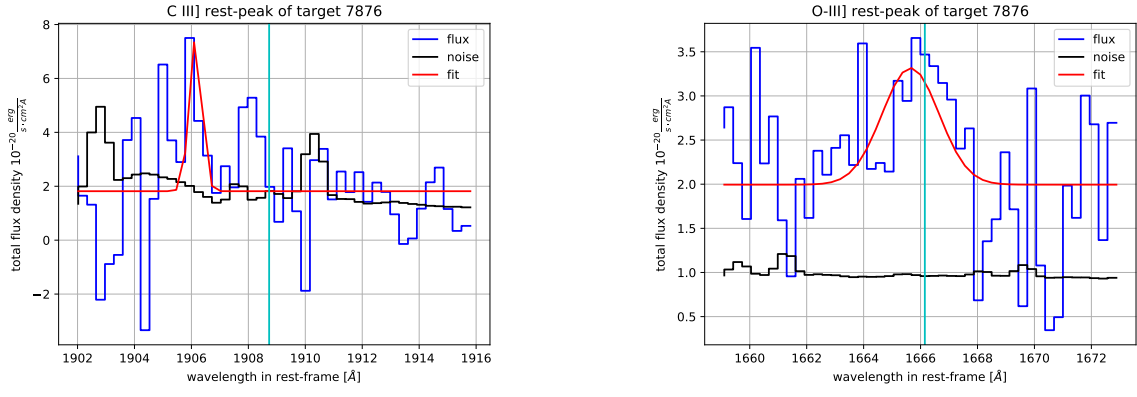Figure 11: O III] λ1666 emission line of target 5199, [27].

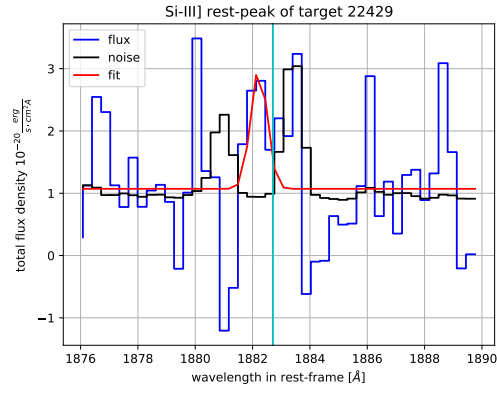Figure 12: O III] λ1666 and C III] λ1909 emission lines of target 7876, [27].

Figure 13: Si III] λ1883 emission line of target 22429, [27].